Dynamics of non-neutral plasmas*

Roy W. Gould†
California Institute of Technology, Pasadena, California 91125

(Received 14 November 1994; accepted 9 January 1995)

In this paper the focus is on the dynamics of two-dimensional cylindrical non-neutral plasmas. After reviewing some highlights of the non-neutral plasma dynamics, some recent two-dimensional results are described: vortex dynamics, diocotron instabilities of hollow profiles, collisionless damping of modes and fluid trapping by modes, fluid echoes, the cyclotron center of mass modes and warm plasma Bernstein modes, and temperature determination from fluctuation measurements. Attention is called to some unsolved problems. © *1995 American Institute of Physics.*

I. INTRODUCTION

A brief chronology of developments in non-neutral plasmas is shown in Table I. Work on non-neutral plasmas goes back at least to the pioneering paper by Brillouin,[1] in which he first described steady-state flows of charged particle beams in a magnetic field, a form of magnetic focusing in which the repulsive space charge electric field E generated by charged particles is balanced by a Lorentz $v \times B$ force of the particles moving through a static magnetic field. He described both planar and cylindrical steady-state flows, illustrated in Fig. 1 for the case of electrons. Both were later used for magnetic focusing of electron beams in various types of microwave devices. One of the earliest attempts to understand the dynamics of such beams was by McFarlane and Hay.[2] In attempting to explain the operation, the highly successful magnetron device, they studied the behavior of small perturbations in a planar Brillouin beam and showed that they could be unstable. Because of the sheared nature of the flow, the instability was termed the slipping stream instability and also the diocotron instability. Attempts to give a quantitative theory of the magnetron were not very successful, but Brillouin flow found important applications in beam-type microwave devices, such as the traveling wave tube[3] (cylindrical beams) and the French M-type backward wave oscillator[4] (planar beams). In these applications, good quantitative theories of the beam dynamics, together with their interaction with slow-wave circuits, were possible.[5] In the case of the M-type backward oscillator, the instability of the thin beam resulted in a reduced start-oscillation current.[6] In the case of magnetically focused hollow beams, the instability resulted in beam breakup.[7] However, most microwave device researchers of the time did not think of their beams as plasmas.

The science of plasma physics began to prosper in the 1960s because of the interest in fusion energy, accelerators, and ion sources. Work on non-neutral plasmas accelerated in the 1970s. The cylindrical Brillouin equilibrium was verified over the entire range of rotational velocities.[8] Charged particles were injected and trapped in magnetic mirror fields.[9] A variety of configurations were devised and studied, both experimentally and theoretically. Considerable attention was given to the equilibria and their stability.[10,11] The diocotron instability was further analyzed and the analogy with two-dimensional (2-D) incompressible inviscid fluid flow was recognized.[10,11] An excellent and comprehensive review of this phase of the non-neutral plasma research is found in the two volumes on non-neutral plasmas by Davidson.[12,13]

Confinement of pure electron and pure ion plasmas using Penning traps became important in the 1970s and developed along two tracks, largely independent at first. Both configurations employ electrostatic fields for axial confinement and are illustrated in Fig. 2.

The Penning trap with hyperbolic electrodes[14] was introduced to contain charged particles for precision spectroscopic measurements. In hyperbolic traps the electrodes are shaped so that the confining potential is proportional to $r^2 - 2z^2$. This makes the orbit of a single particle in the trap particularly simple.[15] In spectroscopic work, plasma effects are undesirable and minimized. There has been very extensive work by the chemists in ion-cyclotron resonance mass spectrometry in traps. Positrons and antiprotons in sizable numbers are trapped, contained, and transported.[16,17] The densities in hyperbolic traps can be made sufficiently high that plasma effects become important and very low temperatures have been achieved by laser cooling.[18] At low temperatures the thermal equilibrium in a quadratic trap potential is a rigidly rotating spheroid of constant density. These states are routinely observed. Dubin[19] has given a theory of the plasma modes of cold spheroidal plasma in the rigid rotor state. These modes are now used as a diagnostic to determine plasma densities, shapes, and temperatures,[20,21] the latter with an extension of Dubin's theory.

Malmberg, Driscoll, and co-workers[22] developed the cylindrical Penning trap to study basic plasma phenomena in a relatively idealized situations. Many phenomena have been identified and studied.[23–27] One of the major developments to come from this line of investigation is the new experimental method for the study of two-dimensional (2-D) vortex dynamics,[24] a subject of longstanding interest in the field of fluid mechanics. A good summary of more recent research on non-neutral plasmas will be found in two AIP Conference Proceedings.[28,29]

The remainder of this paper deals with 2-D phenomena in cylindrical pure electron plasmas, and is organized as fol-

---

*Paper 7RV1, Bull. Am. Phys. Soc. **39**, 1693 (1994).
†Invited speaker.

1070-664X/95/2(6)/2151/13/$6.00

TABLE I. Advances in non-neutral plasmas (the last column indicates references in the text).

1945	Brillouin equilibrium	1
1954	Beams in microwave tubes	3,4,5,6
1965	Hyperbolic ion trap	14
1968	Relativistic beam equilibria	9
1974	Book on non-neutral plasmas	12
1975	Cylindrical electron trap	22,23
1987	Collisional equilibration	25
1989	Vortex dynamics	24,26,27,33,34
1991	Modes of a spheroidal plasma	18,19,20,21
1992	Bernstein modes	46
1994	Collisionless damping and trapping	36

lows. In Sec. II we summarize the Brillouin equilibrium, the 2-D drift-dynamic equations for low frequencies, low densities, and zero temperature. Their similarity with the Euler equations for 2-D inviscid incompressible fluid flow[10,11,23] is reviewed, and a few simple but important, results are cited. In Sec. III we discuss the linearized equations for situations in which the density and angular velocity depend on radius (shear-flow) and instabilities when the density and angular velocity profiles are nonmonotonic. In Sec. IV internal perturbations, collisionless (Landau-like) damping of the response to an applied pulse, and the trapping of fluid elements is discussed. Damping can be understood in terms of phase mixing because of the different angular velocities with which persistent density perturbations are convected at different radii. Experimental evidence is presented for trapping of the fluid by the wave. In Sec. V the possibility of echoes arising out of the nonlinear interaction between two applied pulses is discussed. In Sec. VI we discuss high-frequency (cyclotron) modes, where inertial terms and plasma temperature are important. Finally, in Sec. VII some unsolved problems connected with the above are enumerated.

II. TWO-DIMENSIONAL CYLINDRICAL DYNAMICS AND THE INVISCID FLUID ANALOGY

The Brillouin steady state for a cold cylindrical non-neutral plasma is one in which the inward magnetic force due to the rotational angular velocity cancels the outward electrostatic repulsive force of the charges and the outward centrifugal force at every radius. When the density $n_0(r)$ is independent of the radius, the angular velocity of rotation $\omega_0(r)$ is also independent of radius, the so-called rigid rotor state. The rotation frequency is determined by the force-balance equation,

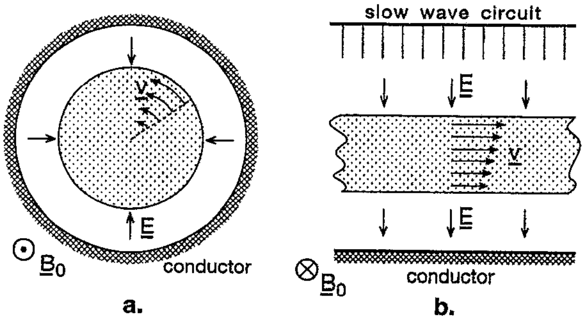

FIG. 1. Brillouin Flow. (a) Cylindrical, (b) planar. (b) is shown with a slow-wave circuit, as used in Backward Wave Oscillators.

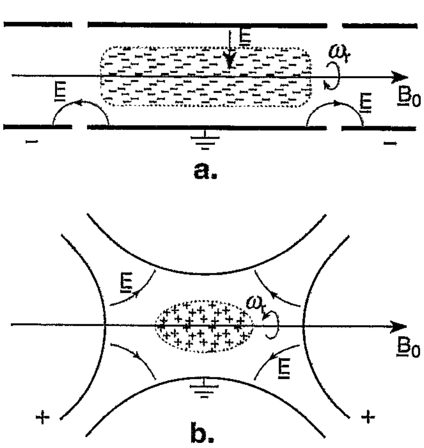

FIG. 2. Penning traps. (a) Cylindrical and (b) hyperbolic. Radial containment is, by the axial magnetic field and axial containment, is electrostatic.

$$\omega_0^2-\omega_0\omega_c+\omega_p^2/2=0, \tag{1}$$

and the solutions of this equation, which are well known, are depicted in Fig. 3, along with experimental data.[8] At the maximum density, $\omega_p^2=\omega_c^2/2$, the Brillouin limit. Most experiments on pure electron plasmas, which will be the focus of this paper, are at low density, in the lower left corner of Fig. 3, where $\omega_p^2 \ll \omega_c^2$. Small-amplitude 2-D perturbations from the rigid rotor steady state are surface waves, traveling around the perimeter $\sim\exp(im\theta-i\omega t)$, as illustrated in Fig. 4. There are discrete low-frequency and high-frequency surface modes:

$$\omega=[m-1+(a/b)^{2m}]\omega_0, \tag{2a}$$

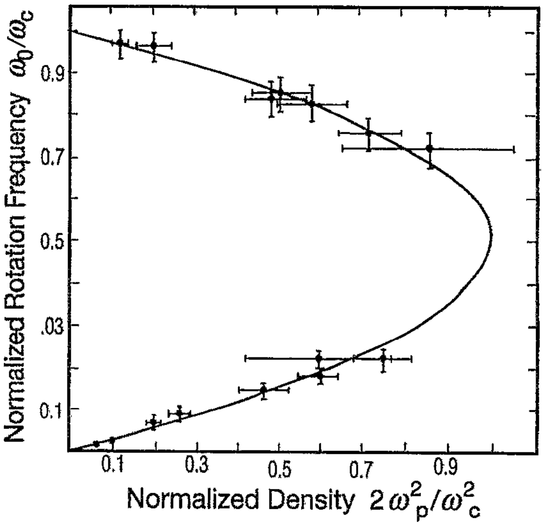

FIG. 3. Rotation frequency versus plasma density in Brillouin equilibrium. Experimental points are from Ref. 8.

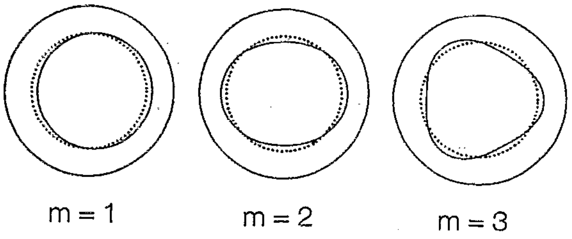

FIG. 4. Surface modes of a cylindrical non-neutral plasma with constant density.

$$\omega=\omega_c+[m-1-(a/b)^{2m}]\omega_0, \qquad (2b)$$

where a and b are the radii of the plasma and a surrounding metal cylinder, respectively. The $m=1$ modes are simple center of mass modes and the sum of their frequencies is ω_c. The frequency of the $m=1$ low-frequency mode, $\omega=\omega_0(a/b)^2$, depends only on the mean density within the cylinder. These modes have no z dependence ($k_z=0$). With z dependence $\sim\exp(ikz)$ the modes propagate in the z direction as well. Axially propagating modes have been analyzed,[12,13,30] and they are similar to the Trivelpiece–Gould modes[31] of a neutral plasma, except that plasma rotation adds a new feature. For $m=0$, plasma rotation does not matter, and the axially propagating modes have been studied experimentally.[22]

For low density and low frequencies the inertial terms can be neglected, e.g., the first term in Eq. (1), and the drift approximation can be used in which the electron fluid velocity is given by $\mathbf{v}=(\mathbf{E}\times\mathbf{B}_0)/B_0^2$. For electrostatic disturbances $\mathbf{E}=-\nabla\phi$, so that $\nabla\cdot\mathbf{v}=0$, and 2-D fluid flow is incompressible. Since $\mathbf{v}=-\nabla\phi\times\mathbf{B}_0/B_0^2$, the flow is along equipotentials and ϕ is, aside from a factor $1/B_0$, the streamfunction. Furthermore, the vorticity (z component) $\nabla\times\mathbf{v}=\nabla^2\phi/B_0$ is, for a pure electron plasma, equal to ne/ϵ_0B_0. The density is related to the velocity by the continuity equation, which, because $\nabla\cdot\mathbf{v}=0$, can be written as $\partial n/\partial t+\mathbf{v}\cdot\nabla n=0$. This means that the density is simply convected with the flow. The fact that these equations have the same form as the Euler equations for an inviscid ordinary (uncharged) fluid was recognized early in the study of non-neutral plasmas.[10] A comparison of the two sets of equations is given in Refs. 11 and 24. Only in the past half-dozen years has this similarity been exploited experimentally. It has produced some beautiful experimental results in 2-D vortex dynamics,[24,25] and made contact with a large body of literature in theoretical and computational vortex dynamics in the field of fluid mechanics.

Perhaps one of the most striking examples is the merger of two vortex patches when their initial separation is less than a critical value, about 1.7 times the diameter of the vortex patch. This was a longstanding prediction in fluid mechanics, but it was first demonstrated experimentally in a definitive manner by Fine *et al.* in a pure electron plasma.[26] This work also provides an excellent example of the ability to image the line-averaged plasma density (proportional to vorticity) when it is dumped.

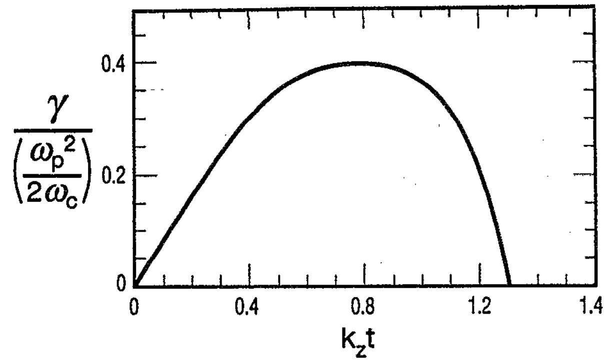

FIG. 5. Growth rate versus thickness for a planar Brillouin beam.

III. RADIAL DENSITY PROFILES AND STABILITY

The instability of the planar beam described in the Introduction has a cylindrical analog. It was first demonstrated experimentally in hollow electron beams by Kyle and Webster.[7] They showed that as the hollow beam propagates, it tends to break up into a number of spiral vortices, the number depending on the thickness of the beam. This is the simplest example of a nonmonotonic density profile: constant density between two radii, r_1 and r_2, and zero for $r<r_1$ and for $r>r_2$. The flow is incompressible and sheared, with the angular velocity of electrons at the outer surface greater than at the inner surface. The stability boundaries for this geometry were determined by Levy.[10] The notion of surface waves, running around the inner and outer surfaces at different velocities, is useful. The wave on the outer surface has negative energy, and the wave on the inner surface has positive energy. If the beam is not too thick (compared with the azimuthal wavelength) the fields of the positive and negative energy surface waves overlap, and their velocities are sufficiently close that they are coupled. This allows them both to grow exponentially. It is easy to show that the growth rate depends on the ratio of the beam thickness to the azimuthal wavelength, and has a maximum,[6,32] as shown in Fig. 5. In experiments where the instability is initiated by noise, the wavelength with the fastest growth rate should be observed, and this decreases with beam thickness. This feature of instability has been nicely demonstrated by Peurrung and Fajans[33] in a cylindrical trap, as shown in Fig. 6.

In the most pure electron plasmas, the radial density distribution is not uniform, though approximately axisymmetric. In this case the angular velocity also depends on radius, and the flow is *sheared*. This significantly increases the complexity and subtlety of the dynamics. The dependence of the angular velocity on the radius is determined by the density through the equation

$$\omega_0(r)=\frac{e}{\epsilon_0B_0r^2}\int_0^r n_0(r')r'\,dr'. \qquad (3)$$

It is convenient to normalize the density and angular velocity profiles to their central values $\omega_0(r)=\omega_0(0)\ f(r)$ and $n_0(r)=n_0(0)\ g(r)$, where $\omega_0(0)=\omega_p^2(0)/2\omega_c$ is the central rotation frequency. Such profiles are expected to evolve to the rigid rotor steady state, but in many experiments the time

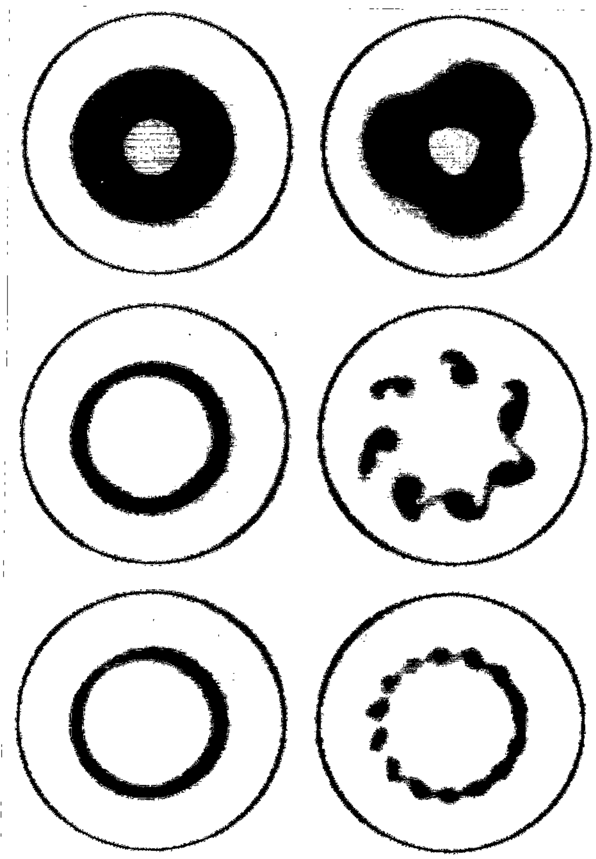

FIG. 6. Images of unstable hollow plasmas showing the azimuthal wavelength for three thicknesses (0.67, 0.17, and 0.14 cm). Left side: before instability; right side: after onset (from Ref. 33).

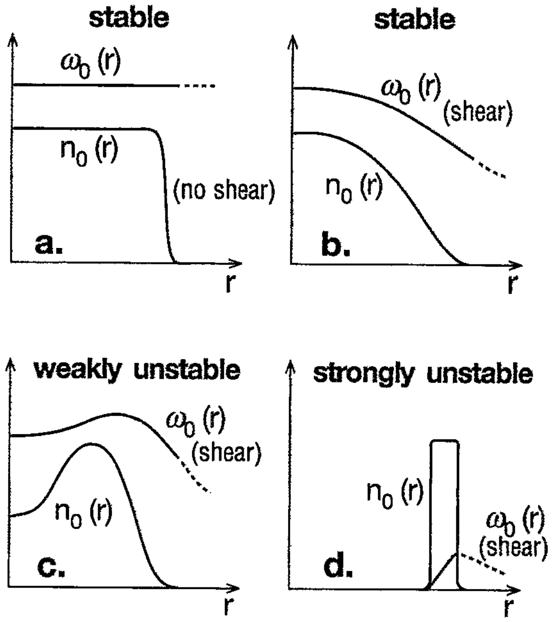

FIG. 7. Density profiles and corresponding angular velocity profiles, monotonically decreasing and stable (upper), and hollow profiles that are unstable (lower).

to do so is too long for this to be achieved. This evolution is sufficiently slow that, for most oscillation and wave phenomena, the profiles can be regarded as steady. Examples of monotonic and nonmonotonic density profiles and the resulting angular velocity profiles that will be discussed in this paper are shown in Fig. 7. The last of these, Fig. 7(d), is the hollow beam described briefly above.

For this paper we are interested in the smooth profiles shown in Fig. 7(b) and Fig. 7(c). Linear modes of these profiles have many similarities with (and some differences from) longitudinal plasma waves in a Vlasov plasma. In Ref. 11, smooth profiles were examined, and it was shown that a necessary condition for instability (the existence of a temporally growing eigenmode) of such a system is that $dn_0(r)/dr$ change sign, i.e., that the profile is nonmonotic, such as shown in Fig. 7(c). This is not a sufficient condition, however. Figure 7(c) depicts (approximately) the profile used in the experiment of Driscoll *et al.*,[34] which demonstrated that the $m=2$ mode was unstable. In that work, a small seeded $m=2$ perturbation was seen to grow exponentially from the linear regime and to form two vortices (density clumps) that eventually merge, as illustrated in Fig. 8.[34] Eventually, the high-density annulus ends up in the center, and the density profile becomes, in a coarse grain sense, monotonically decreasing.

This situation was also studied[34] with a 2-D fluid code, which solved the nonlinear equations described in Sec. II on a 256×256 square grid on which the potential at all points outside an inscribed circle, corresponding to the conducting wall, was set to zero. A successive over-relaxation Poisson solver was used and the density was advanced in time using a 15 point Arakawa algorithm.[35] The density at six times in the evolution, corresponding to about 20 rotation times of the column is shown in Fig. 9. The first "frame," where the $m=2$ perturbation of the annulus is hardly visible, is in the linear regime. By the third frame the two large vortices have formed, and in the fourth frame they are beginning to merge. Two density holes persist near the edge for some time. Re-

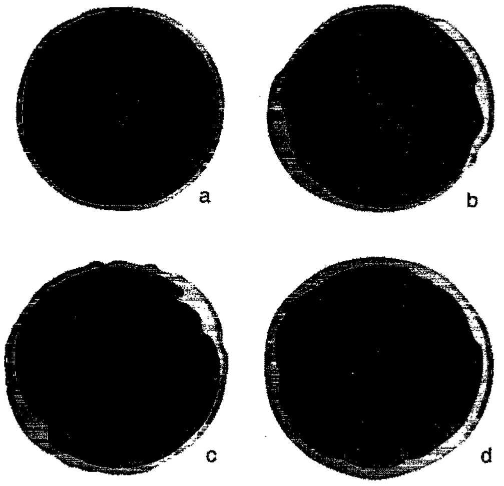

FIG. 8. Measured z-averaged density $n(r,\theta)$ at $t=50$, 120, 170, and 1000 μs (a)–(d), as $m=2$ hollow profile instability grows, saturates, and evolves to a stable monotonic profile. The darkest areas correspond to the highest density (from Ref. 34).

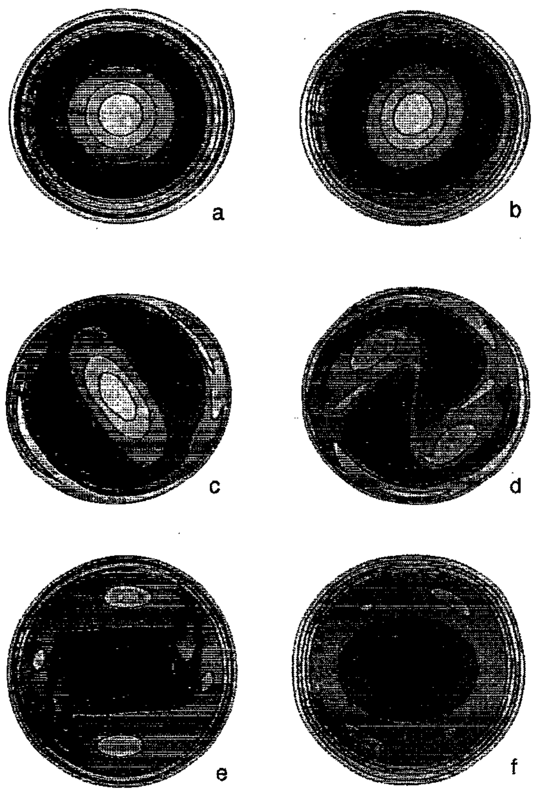

FIG. 9. The fluid code calculation of $n(r,\theta,t)$ at six successive times (a)–(f) in the evolution of the $m=2$ hollow profile instability. The darkest areas correspond to the highest density.

cently, Huang has shown that the asymptotic (late time) experimental density profile is reasonably well fit by a minimum enstrophy theory rather than a maximum entropy theory.[27]

IV. CONTINUUM OF MODES, COLLISIONLESS DAMPING, AND FLUID TRAPPING

Before describing experimental results on collisionless damping and trapping,[36] we review the linear theory of disturbances in stable profiles, following an approach similar to that in Ref. 11. We use the usual notation for unperturbed and perturbed quanties, denoting them by subscripts 0 and 1, respectively, and we assume angular dependence of $\exp(im\theta)$. The linearized Poisson's equation becomes

$$\frac{d^2\phi_1}{dr^2}+\frac{1}{r}\frac{d\phi_1}{dr}-\frac{m^2}{r^2}\phi_1=\frac{n_1 e}{\epsilon_0}, \tag{4}$$

and the linearized continuity equation becomes

$$\frac{\partial n_1}{\partial t}+im\omega_0 n_1-\frac{im}{rB_0}\frac{dn_0}{dr}\phi_1=0, \tag{5}$$

where we have used the drift equation $\mathbf{v}_1=\mathbf{B}_0\times\nabla\phi_1/B_0^2$, the fact that $v_0=r\omega_0$ is in the θ direction, the nonlinear term $v_1\cdot\nabla\, n_1$ has been neglected. Here $n_0(r)$ is assumed to be known and $\omega_0(r)$ is determined from it by Eq. (3). One can write the solution of Eq. (4) as

$$\phi_1(r)=-e\int_0^b G_m(r,r')n_1(r')2\pi r'\,dr'+\phi_{1\,\mathrm{ext}}, \tag{6}$$

where $G_m(r,r')$ is the Green's function for the problem with $\phi_1(0)=\phi_1(b)=0$. In Eq. (6) the potential is split into the part produced by the plasma and the externally applied part. Here $\phi_{1\,\mathrm{ext}}$ is the vacuum potential due to the voltages applied to the conducting wall at $r=b$.

There are two types of problems that one might want to solve: (a) an initial value problem where the initial density $n_1(r,0)$ is given, and one wants to know how the density, potential, etc. evolve subsequently in time, or (b) a situation where a voltage pulse is applied to a segment of the conducting electrode at $t=0$ when the plasma is otherwise undisturbed, and one wants to know how the plasma responds to the pulse. A Laplace transform with respect to time is suitable for either type of problem. In the latter case, $n_1(r,0)=0$ and Eqs. (4) and (5) become

$$\frac{d^2\Phi_1}{dr^2}+\frac{1}{r}\frac{d\Phi_1}{dr}-\frac{m^2}{r^2}\Phi_1=\frac{N_1 e}{\epsilon_0} \tag{7}$$

and

$$(\omega-m\omega_0)N_1=-\frac{m}{rB_0}\frac{dn_0}{dr}\Phi_1, \tag{8}$$

where $\Phi_1(r,\omega)$ and $N_1(r,\omega)$ are the Laplace transforms of the potential and density. We use, for the Laplace variable, $s=-i\omega$, with ω in the upper half-plane. Eliminating N_1 gives

$$\frac{d^2\Phi_1}{dr^2}+\frac{1}{r}\frac{d\Phi_1}{dr}-\frac{m^2}{r^2}\Phi_1+\frac{em}{rB_0\epsilon_0}\frac{dn_0/dr}{(\omega-m\omega_0)}\Phi_1=0. \tag{9}$$

This equation has been extensively studied. Briggs *et al.*[11] were the first to give a general discussion of the analytic properties of Φ_1 in the complex ω plane and note the similarity of this situation with that of Landau damping of longitudinal plasma waves. Here $\Phi_1(r,\omega)$ and $N_1(r,\omega)$ are defined in the upper-half ω plane. As the real ω axis is approached from above, the denominator of Eq. (9) becomes singular if the real part of ω lies in the range

$$m\omega_{0\,\min}<\mathrm{Re}\{\omega\}<m\omega_{0\,\max}, \tag{10}$$

where $\omega_{0\,\min}$ and $\omega_{0\,\max}$ are the minimum and maximum rotation frequencies in the plasma. This gives rise to a branch line along the real frequency axis between these limits, as shown in Fig. 10(a). The potential function can be analytically continued into the lower half-plane, as discussed in Ref. 11, leading to the deformed contour of Fig. 10(b).

As with Langmuir waves, one can show that Eq. (9) has a continuum of singular eigenmodes (generalized functions) in the frequency range given by Eq. (10), similar to the Van Kampen–Case modes[37,38] for Langmuir oscillations. This leads to two complementary views, or descriptions, of collisionless damping, which are equally valid. Although the diocotron mode problem is similar in many ways to the Landau problem,[39] it is different in two significant ways: the frequency range is limited by Eq. (10) and each (angular) velocity is associated with a *different radius*.

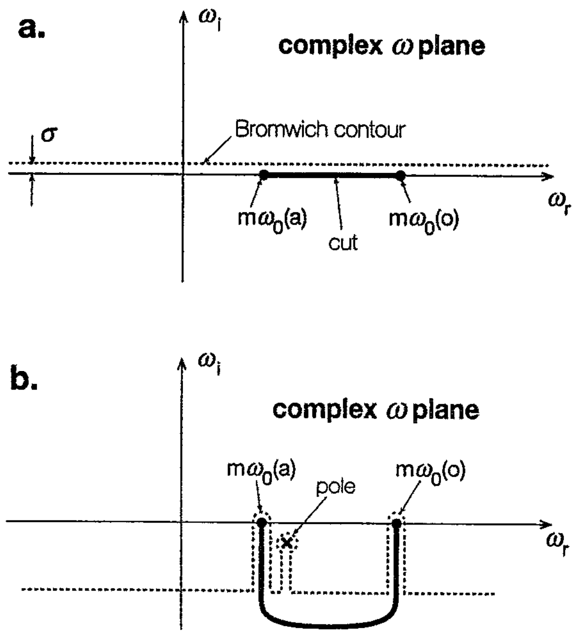

FIG. 10. (a) The Bromwich contour in the complex ω plane used in inverting the Laplace transform. (b) Deformed contour revealing the simple pole in the lower half-plane.

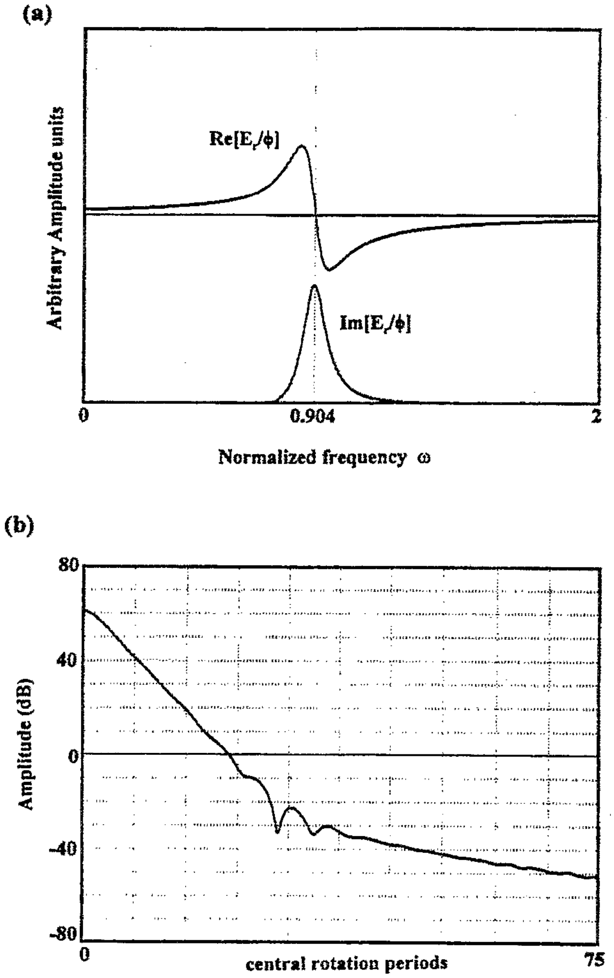

FIG. 11. (a) Real and imaginary parts of $(E_{r1}/\phi_1)_{r=b}$ as a function of frequency normalized to the central rotation frequency, for $m=2$. The vertical dotted line corresponds to the $m=2$ resonant frequency, $\omega=0.904\omega_0(0)$, for this profile. (b) The semilog plot of the envelope of the inverse transform of $(E_{r1}/\phi_1)_{r=b}$. The initial decay changes from exponential to algebraic (from Ref. 36).

For comparison with experiment[36] we are primarily interested in the response of the plasma to an applied pulse. We need solutions of Eq. (9) in which $\Phi_1(b,\omega)$, the Laplace transform of the potential at the conducting wall is equal to the applied potential. Here Φ_1 must vary as r^m near the origin. To compare with experiment we need the radial electric field at $r=b$ from which the charge induced on the wall can be obtained. For special profiles of the form, $f(r)=1-(r/b)^{2n}$, Corngold[40] has shown that the solution of Eq. (9) can be expressed in terms of the hypergeometric function, and the location of the pole illustrated in Fig. 10(b) can be determined analytically.

We are interested in more general profiles, $n_0(r)$ and $\omega_0(r)$, where solutions are not necessarily expressible in terms of known functions. Our approach is to numerically integrate Eq. (9) with respect to r for a specific density profile and for a discrete set of equally spaced frequencies ω_k along the contour shown slightly above the real frequency axis in Fig. 10(a). We obtain the temporal response (wall charge) from an inverse Discrete Fourier Transform (DFT) of $\epsilon_0|\partial\Phi_1(r,\omega_k)/\partial r|_{r=b}$. To compare with experimental measurements the admittance function[36] is defined by

$$Y(\omega)=+i\omega 2\pi\epsilon_0 F_1 F_2\left|\frac{r[\partial\Phi_1(r,\omega)/\partial r]}{\Phi_1(r,\omega)}\right|_{r=b}, \tag{11}$$

where F_1 and F_2 are form factors of the sectorized wall conductor. The admittance function is the Fourier transform of the current response in sector 2, due to an impulse applied to sector 1. For the smoothness of this function, there is a requirement that the ratio of the step size in the radial integration and the step size in frequency satisfy the inequality $\Delta r \ll \Delta\omega/(d\omega_0/dr)$. Evaluation of transform functions at frequencies at a distance σ slightly above the real frequency axis, followed by taking its inverse with a DFT, which assumes ω to be real, gives rise to an additional exponential damping factor, $e^{-\sigma t}$, which can easily be corrected for. The real and imaginary parts of the principal factor in the admittance function, $(rE_{r1}/\Phi_1)_{r=b}$, are shown for a typical monotonic density profile and for $m=2$ in Fig. 11. Also shown in Fig. 11 is the $m=2$ impulse response obtained from the inverse DFT of $(rE_{r1}/\Phi_1)_{r=b}$. The admittance has a nonzero real part only in the frequency range described by Eq. (10) when there is a resonance in the denominator of Eq. (9). The admittance function is defined so that $\mathrm{Re}\{Y(\omega)\}>0$ corresponds to absorbtion. Since $\mathrm{Re}\{Y(\omega)\}<0$ in this frequency range, energy is *released* when a disturbance is excited, so the system is a negative energy system.

The real and imaginary parts of $(rE_{r1}/\Phi_1)_{r=b}$ shown in Fig. 11 can be approximated by a simple pole below the real frequency axis plus a small remainder function,

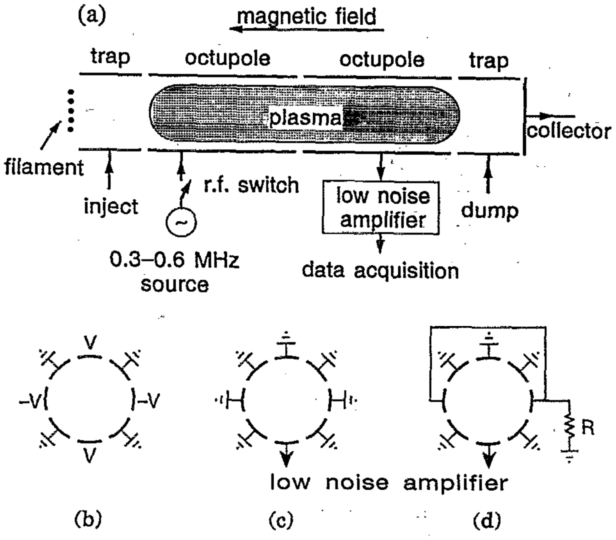

FIG. 12. (a) Schematic of a cylindrical structure for plasma excitation and trapping, (b) the phasing of a first octupole for exciting an $m=2$ disturbance, (c) the configuration of the second octupole for signal reception, and (d) the configuration of the second octupole for the negative energy test (from Ref. 36).

$$Y(\omega)=\frac{i\omega B}{(\omega-\omega_2+i\gamma_2)}+\Re(\omega), \tag{12}$$

where B is negative because of the negative energy property. Equation (12) is consistent with Fig. 10(b), which shows a simple pole below the real frequency axis. Here $\Re(\omega)$ comes from integrals along the branch cuts. The exponential decay that dominates the early time behavior is associated with the pole and the algebraic decay that appears later is associated with $\Re(\omega)$. While the precise details of behavior of $(rE_{r1}/\Phi_1)_{r=b}$ or $Y(\omega)$, and thus of the impulse response, are profile dependent, the general features are the same for qualitatively similar profiles. The frequency ω_2 corresponds to twice (because $m=2$) the rotational angular velocity at a radius r_s near the outer limit of the plasma (~0.8× the plasma radius).

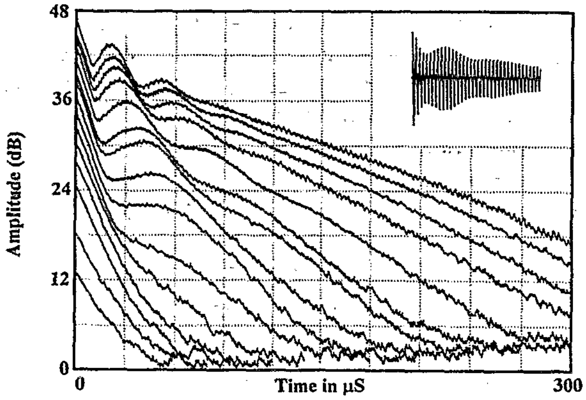

FIG. 13. Decay of the envelope of the $m=2$ signal at about 400 kHz excited by the rf pulse with voltages 10 (lower left), 20, 40, 60, 80, 120, 160, 200, 250, 300, 400, 500, 600, 700, and 1000 (uppermost) mV, plotted on a semi-log scale with a vertical scale (from Ref. 36).

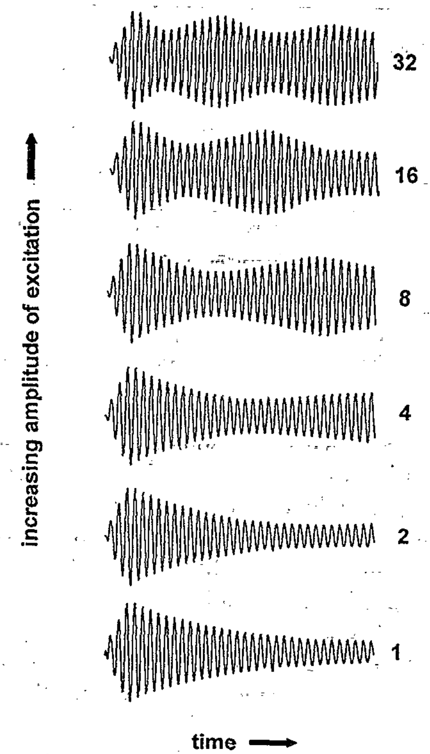

FIG. 14. The 2-D fluid code calculation of damping and trapping. Plotted is the charge induced on one octant of the cylinder, and in each successive trace the excitation amplitude is doubled and the vertical scale is halved (from Ref. 41).

Collisionless damping of the $m=2$ mode in the linear regime has recently been observed by Pillai[36] using the experimental apparatus depicted in Fig. 12. The *envelope* of the decaying sine wave, which is excited by a 5 μs sinusoidal burst (about three cycles), is shown in Fig. 13 for various amplitudes of the burst. Each trace is the average of 20 "identical" traces, and an example of an actual sinusoidal signal is shown in the inset. The lowest three traces are essentially in the linear regime. As the amplitude of the excitation is increased, "bounce" oscillation begin to appear, indicating trapping of the fluid near the resonant layer. An analysis of the bounce frequency, when corrected for decay of the wave amplitude, shows that it is proportional to the square root of the applied voltage. Trapping in fluids in shear flow was anticipated by Kelvin, with his "cats eyes" describing fluid trajectories. In Ref. 11 it was predicted that the "bounce" or trapping frequency should be given by

$$\omega_b \approx m\sqrt{|\Phi_1\omega_0'(r)/r|_{r_s}/B_0}.$$

Pillai[36] observes that the bounce frequency is proportional to the applied potential to the power 0.55±0.10 using 22 datasets. Using the 2-D fluid code described earlier, both collisionless damping and amplitude modulation of the decaying wave due to trapped particles have been verified.[41] Figure 14 shows a calculation using this fluid code of the charge induced on one octant of the conducting cylinder when a three-cycle sinusoidal burst is applied. The linear decay rate agrees well with that obtained by numerical solution of the linear differential equation and the bounce fre-

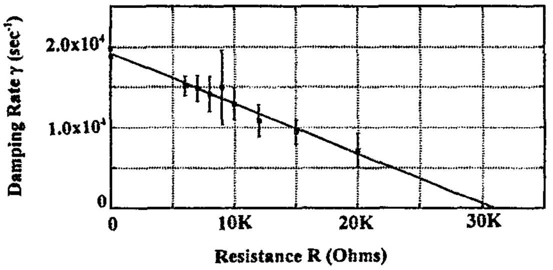

FIG. 15. A decrease in the decay rate of the $m=2$ response versus resistance when a resistance R is connected to the wall sectors, as shown in Fig. 12(d). The line is a least squares fit to the experimental data (from Ref. 36).

quency is proportional to the square root of the amplitude. deGrassie[23] first looked for linear collisionless damping, but his detection sensitivity did not allow him to study the linear regime. Instead, he found a much slower decay whose rate decreased with increasing amplitude, much like the late time behavior in Fig. 13. He also failed to see the bounce motion.

The negative energy feature of the perturbations has an interesting consequence. When energy is removed from the system, by external resistors, for example, the amplitude should grow. This was previously established for the $m=1$ center of mass mode by White, Malmberg, and Driscoll.[42] For $m>1$, however, the modes are already damped by the collisionless phase mixing process just described. When external resistors are added, as shown in Fig. 12(c), the collisionless damping rate of the $m=2$ mode is *decreased.* Figure 15 shows the damping rate versus resistance. Furthermore, with sufficient external dissipation the otherwise damped mode can be turned into a growing mode.

By examining the electric field at the conducting wall we have seen that the linear response to a short applied pulse is a decaying sinusoid, approximately exponential. However, density perturbations at each radius within the plasma persist indefinitely in the ideal drift approximation. This can be seen by inverting Eq. (8),

$$n_1(r,t)=\frac{-m}{rB_0}\frac{dn_0}{dr}\int\frac{\Phi_1(r,\omega)}{[\omega-m\omega_0(r)]}e^{-i\omega t}\frac{d\omega}{2\pi}, \tag{13}$$

which, because of the simple pole at $\omega=m\omega_0(r)$ gives an undamped contribution to $n_1(r,t)$ proportional to $\exp[-im\omega_0(r)t]$. Thus, perturbations at each radius continue to be convected, undamped, at the local angular velocity. The density $N_1(r,\omega)$ and $n_1(r,t)$, calculated by the numerical methods described above, is shown for several representative radii in Fig. 16. It is seen that $n_1(r,t)$ does not decay [Fig. 16(b)], but has different frequencies [Fig. 16(a)] at different radii. However, the electric field at the conductor (and therefore the charge on the conductor) decays away, because it is caused by (a weighted average of) charge density perturbations at various radii. This result is expressed mathematically as the derivative with respect to r of the *integral* in Eq. (6). Because of the radially dependent phase factor in the integrand, contributions from different radii have different frequencies and phase mix away. The initial and phase mixed density perturbations are illustrated in Figs. 17(a) and 17(b), respectively.

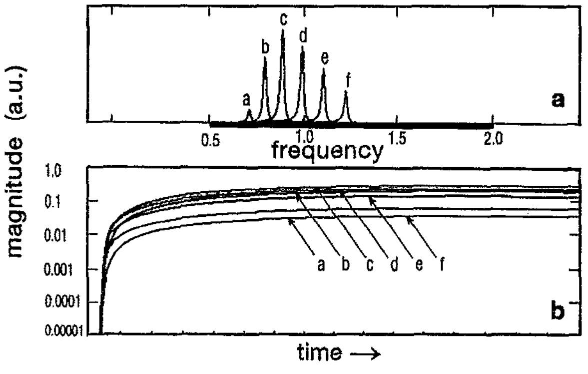

FIG. 16. Density perturbations at $(r/a)=0.93$, 0.87, 0.81, 0.75, 0.69, and 0.63 (traces a–e). (a) Magnitude of the Laplace transform of the density versus frequency along the contour in Fig. 10(a). (b) A semilog plot of the magnitude of density versus time at the various radii.

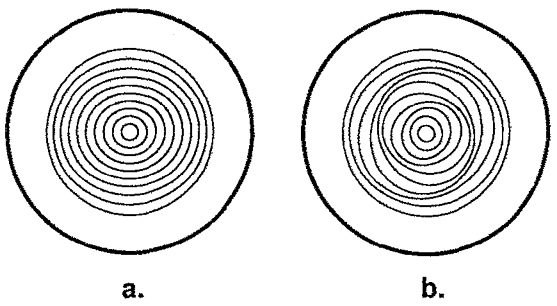

FIG. 17. The internal $m=2$ perturbation of cylindrical non-neutral plasma. (a) Density contours when perturbations at all radii are in phase and (b) after phase mixing.

V. FLUID ECHOES

The dynamics of the ideal fluid is time reversible and one suspects, by analogy with the cyclotron echoes[43] and plasma wave echoes,[44] that this system might also exhibit echoes. The application of a second pulse might partially unmix the undamped phase-mixed remnants of the first pulse, and create a coherent response at a later time, long after the responses to both pulses have decayed away. The mixing occurs because of different *angular* velocities so, by analogy with the plasma wave echo, we examine the effects of two pulses applied to the electrode structure shown in Fig. 12. The connections are arranged so as to produce potentials with different angular dependences: m_1 for the first pulse and m_2 for the second pulse. For simplicity, the time dependence of the applied pulses are taken to be $V_1t_1\delta(t)$ and $V_2t_2\delta(t-\tau)$, respectively. This form serves as the Green's function (in time) for other pulse shapes. The following notation is used:

$$\phi=\phi_0(r)+\phi_1(r,t)+\phi_2(r,t)+\phi_3(r,t), \tag{14a}$$

$$n=n_0(r)+n_1(r,t)+n_2(r,t)+n_3(r,t), \tag{14b}$$

where the subscript 0 refers to the steady state, subscripts 1 and 2 refer to the first and second applied pulses, and subscript 3 refers to the echo. The echo results from the nonlinear interaction between pulses 1 and 2. We treat the first and second pulses in the linear approximation (as described above), and seek the nonlinear interaction between the two pulses to obtain the echo response to *second* order in the amplitudes. To this order the continuity equation for the echo may be written as

$$\frac{\partial n_3}{\partial t}+\omega_0\frac{\partial n_3}{\partial \theta}+v_{3r}\frac{dn_0}{dr}=-v_{2r}\frac{\partial n_1}{\partial r}-\frac{v_{2\theta}}{r}\frac{\partial n_1}{\partial \theta}-v_{1r}\frac{\partial n_2}{\partial r}-\frac{v_{1\theta}}{r}\frac{\partial n_2}{\partial \theta}, \qquad (15)$$

where the nonlinear terms arising out of the interaction of the pulses 1 and 2 have been put on the right-hand side. These terms, which will be denoted by $s_3(r,t)$, act as *source* terms for the echo, and are obtained from the linear solutions for pulses 1 and 2. The left-hand side is the usual linearized continuity equation.

Since we are using complex exponentials to describe quantities that are real and, by convention, taking the real part (or adding the complex conjugate and dividing by 2), some care is required with the quadratic source term. Since the source term $s_3(r,t)$ consists of *products* of time-dependent quantities, the transform of s_3 is given by the *convolution* of the transforms of the individual quantities. Also, the complex conjugate of one of the transforms should be used. We do this for pulse 1, so that the echo has angular mode number $m_3=m_2-|m_1|>0$. Of the four terms in s_3, the first dominates because $n_1(r,t)$ contains terms proportional to $\exp[-im_1\omega_0(r,t)]$, unlike $v_1(r,t)$. Because it is differentiated with respect to r, it contains terms that grow with t. In transform space, the source term has the form

$$S_3(r,\omega)\approx\frac{-im_2}{rB_0}\int \Phi_2(r,\omega-\omega')\,\frac{dN_1(r,\omega')}{dr}\,\frac{d\omega'}{2\pi}, \qquad (16)$$

in the dominant term approximation.

We now describe the method of solution. Equations (7) and (8) must be solved, for a specified density profile, to obtain $\Phi_1(r,\omega)$, $N_1(r,\omega)$, $\Phi_2(r,\omega)$, and $N_2(r,\omega)$ for pulses 1 and 2. Analytic solutions can only be obtained for special profiles, so we resort to numerical methods and consider discrete values of r and ω, $r_j=j\,\Delta r$, and $\omega_k=k\,\Delta\omega+i\sigma$. In particular, we use 512 or 1024 discrete values of ω, so as to use DFTs to obtain the time functions. For each of the discrete values of ω, we numerically integrate Eqs. (7) and (8) from $r=0$ to $r=a$ using a fourth-order Runge–Kutta method, so as to obtain values of the functions at 500 radial points within the plasma. Since we also need $\partial N_1(r,\omega)/\partial r$, it is also calculated during the numerical integration at the 500 radial points. The potentials so obtained must vary as $(r)^{m_1}$ and $(r)^{m_2}$ near the origin and match the Laplace transforms of the applied potentials at the cylinder, respectively. The convolution, Eq. (16), is then done numerically to obtain $S_3(r_j,\omega_k)$. The equations for the echo pulse are similar to those of pulses 1 and 2, except that instead of being driven by potentials applied to the conducting cylinder, the source term is S_3:

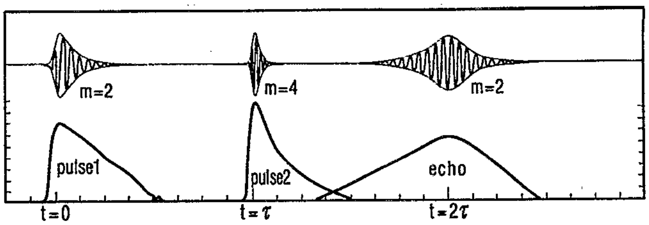

FIG. 18. Time dependence of the response to two applied pulses: $m=2$ at $t=0$ and $m=4$ at $t=\tau$, followed an $m=2$ echo at $t=2\tau$. Upper curve: Waveforms of the electric field at the wall; lower curve: semilog plot of the magnitudes of waveforms. The echo amplitude has been increased for clarity.

$$\frac{d^2\Phi_3}{dr^2}+\frac{1}{r}\frac{d\Phi_3}{dr}-\frac{m_3^2}{r^2}\Phi_3=\frac{N_3e}{\epsilon_0}, \qquad (17)$$

$$(\omega-m_3\omega_0)N_3=-\frac{m_3}{rB_0}\frac{dn_0}{dr}\Phi_3+iS_3. \qquad (18)$$

These are also integrated numerically in radius for 512 discrete frequencies and inverted with a DFT to obtain the time dependence. Figure 18 shows the response to pulses 1 and 2, as well as the echo for a typical profile. Here $m_1=2$, $m_2=4$, and $m_3=2$. In each case the time-dependent electric field at the wall is shown. The echo amplitude is proportional to the product of the amplitudes of pulses 1 and 2, $V_1t_1V_2t_2$, is generally much smaller than the responses to the two pulses. The echo is not shown to scale in Fig. 18.

The echo amplitude is expected to be diminished by viscous effects, as the time between the first pulse and the echo lengthens. This is because perturbations at nearby radii have been convected by substantially different amounts in azimuth, causing the radial gradients to become very large. Thus, the echo phenomenon may form the basis for studying viscous effects. However, the particles primarily responsible for the echo are restricted to the outer radii of the plasma, so that is probably the only region that could be probed.

VI. HIGH-FREQUENCY MODES

So far the discussion has been limited to low frequencies, where the drift approximation is valid. The 2-D modes near the cyclotron frequency also exist, whose frequency is given by Eq. (2b) for uniform density (the rigid rotor steady state). The $m=1$ center of mass mode lies *below* the cyclotron frequency by the diocotron frequency, and the higher modes are upshifted by the rotation of the plasma. Again, this section focuses on nonuniform density and angular velocity profiles, such as shown in Fig. 7(b). Inertial terms can no longer be neglected, and expressions for the fluid velocity in a nonuniformly rotating fluid become much more complicated.

An analysis of the high-frequency behavior,[45] near the cyclotron frequency, of a cold nonuniformly rotating pure electron plasma has been carried out. The mode structure and the admittance function $Y(\omega)$, as defined in Sec. IV, has been evaluated for a number of stable monotonic profiles. The results are not unlike those for the low-frequency diocotron

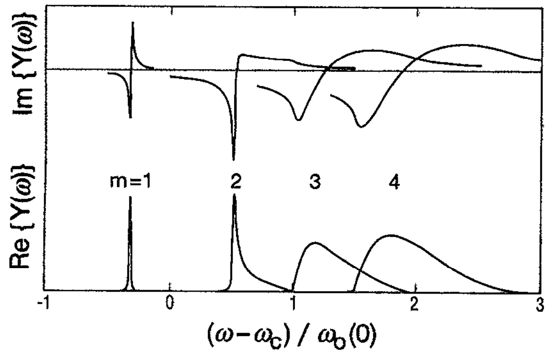

FIG. 19. The real and imaginary parts of the admittance function versus frequency for high-frequency modes ($T=0$). When $\mathrm{Re}\{Y(\omega)\}>0$ absorption occurs due to an upper hybrid resonance somewhere within the plasma. Absorption bands are upshifted by rotation (from Ref. 41).

modes described in Sec. IV. For $m=1$ there is a single discrete mode lying slightly below the cyclotron frequency,

$$\omega=\omega_c-\langle\omega_p^2\rangle/2\omega_c. \tag{19}$$

For each m greater than 1 there is an *absorption* band,

$$(m-1)\omega_0(a)<(\omega-\omega_c)<(m-1)\omega_0(0), \tag{20}$$

upshifted from the cyclotron frequency by the Doppler effect of rotation. As with the low-frequency modes, an alternative point of view is that the absorption band is associated with continuum of singular normal modes. A typical result for the cold plasma admittance function is shown in Fig. 19. These are positive energy modes, as demonstrated both theoretically and experimentally.

Experimentally, the $m=1$ discrete mode is found, as expected, below the cyclotron frequency, but the $m>1$ absorption bands are not found.[46] Instead, in the parameter range where the absorption bands are expected from the cold plasma theory, a set of discrete modes for each m greater than 1 is found. Figure 20 shows a two-dimensional scan in density (horizontal axis) and magnetic field (the vertical axis). The modes for $m>1$ have been interpreted as radially trapped (by the density and angular velocity profiles) azimuthally propagating Bernstein modes.[47] Bernstein modes arise out of finite-temperature (finite Larmor radius) effects, which were not included in the cold plasma rotating fluid analysis. However an *approximate* modification of the theory, which includes electron temperature, has been given,[45,46] and the temperature required to match the experimental observations is consistent with other determinations of plasma temperature (0.5–2.0 eV).

For $m>1$ the effect of plasma temperature is to turn the continuous absorption band described by Eq. (20) into a band in which Bernstein modes can propagate. This is similar, in a general way, to the effect of temperature on the modes of a *neutral* plasma column: Tonks–Dattner modes,[48] which are propagating Langmuir oscillations trapped by the radial density profile. Similarly, in a magnetized neutral plasma, the Buchsbaum–Hasegawa modes[49] near the second harmonic of the cyclotron frequency, arise from Bernstein waves that are trapped because of the radial density gradient. In both cases the inclusion of temperature raises the order of the differential equation and results in additional "thermal" modes in the region where there would otherwise be a continuum of singular eigenmodes.

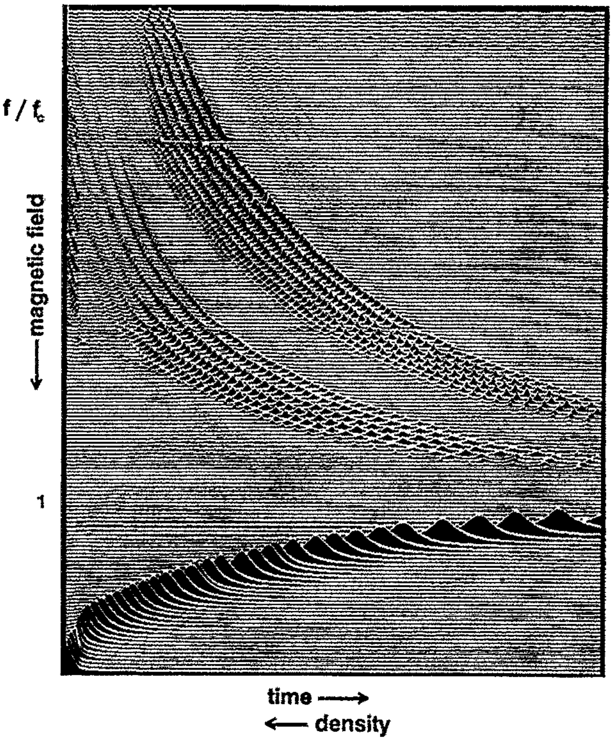

FIG. 20. The experimental scan of $k=0$ modes near the cyclotron frequency in which f/f_c varies by a few percent. There is a single $m=1$ center of mass mode below the cyclotron frequency, and bands of $m=2$ and $m=3$ Bernstein modes above.

In the remainder of this section we concentrate on the $m=1$ center of mass mode, whose frequency is just below the cyclotron frequency. We describe a measurement of spontaneous thermal excitation of this mode and a method for using fluctuation measurements to determine electron temperature. The method consists of measuring the noise power delivered to a low noise receiver caused by the fluctuating currents that are induced on the sector electrodes surrounding the plasma, which are associated with thermal excitation of the $m=1$ mode. The received power is compared with the power from a calibrated reference noise source, and the ratio of the powers is denoted by p. The absorbtion coefficient, A, is also required to determine the temperature. This procedure results in a nondestructive method of temperature determination for pure electron plasmas. In related measurements, spontaneous emission associated with the $m>1$ Bernstein modes has also been observed, and the inferred temperatures are in the same range, although these measurements are subject to greater shot-to-shot irreproducibility. Our method is a variation on the method used by Stenzel[50] for neutral afterglow plasmas, and is related to the stored ion calorimeter discussed by Wineland.[51] These situations differ drastically from the usual radiation transport regime in astrophysics and in fusion devices, where radiation is emitted and absorbed over many wavelengths. This radiation also differs markedly from Larmor radiation from a col-

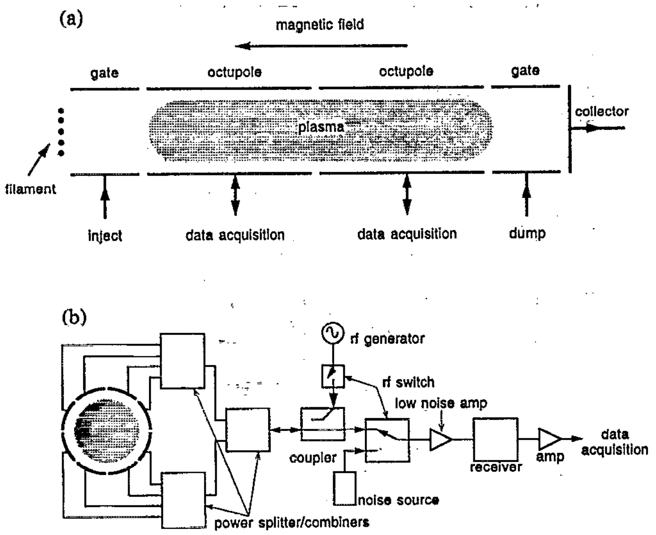

FIG. 21. Schematic for the measurement of radiation temperature from the $m=1$ mode. Emission and absorption are measured on alternate shots and before and after the emission measurement, a comparison with a calibrated noise source is made.

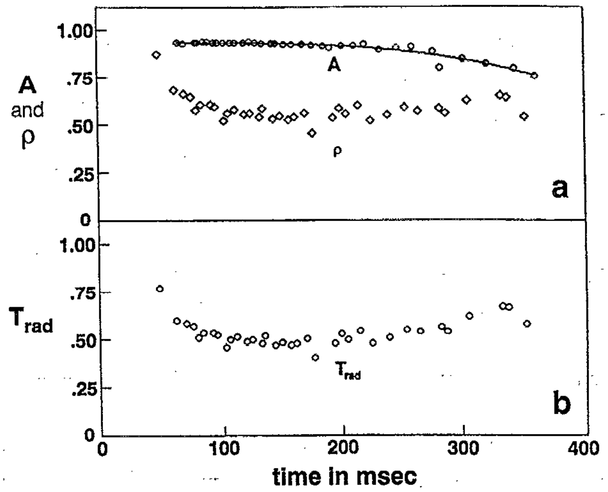

FIG. 23. (a) Emission and absorption versus time. (b) Temperature versus time. Here 35 traces similar to those shown in Fig. 22 have been used.

lection of independent single particles, since only a single collective mode of the plasma is involved.

A schematic diagram of the experimental configuration is shown in Fig. 21. To increase the sensitivity to the noise fluctuations, the signals from all eight sectors of an octupole section are combined, with phasing so as to be sensitive to the $m=1$ mode, and sent to a low noise (noise figure ≈ 3 dB) 140 MHz receiver whose bandwidth is 12 kHz. The cyclotron frequency is set slightly above the receiver frequency, so that, as the plasma density decays, the $m=1$ mode frequency *sweeps upward through* the receiver frequency. By incrementing the magnetic field, and thus the cyclotron frequency, by a small amount on successive shots, the $m=1$ mode resonance can be made to sweep through the receiver frequency at various times in the plasma decay. Time-dependent emission and reflection measurements [the latter using the radio frequency (rf) generator] are made on alternate shots. This is illustrated in Fig. 22, which shows both the noise emission and the reflected power (inverted trace) as a function of time for three representative different values of the magnetic field. At the beginning and end of an emission trace, the receiver is switched briefly to the reference noise source at temperature, T_{ref}. All elements of the measurement system are 50 Ω coaxial components and the insertion loss of all elements must be accounted for.

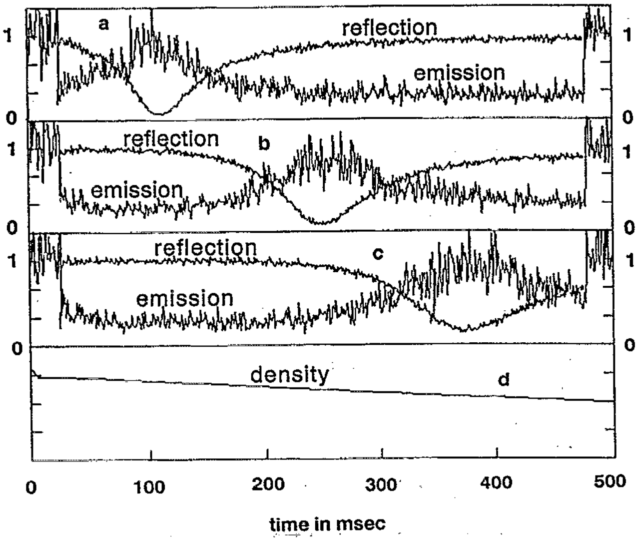

FIG. 22. (a)–(c) Emission and reflection traces versus time. As the density decays the resonance sweeps through the receiver frequency, and by changing the magnetic field slightly, the resonance can be positioned at various times. (d) A semilog plot of density versus time. Each tick mark is a factor of 10.

Typical experimental results: emission, absorbtion, and radiation temperature, are shown in Figs. 23(a)–23(b). These are obtained by fitting Lorentzian curves to the type of data shown in Fig. 22, and using the *maximum* values. The results from about 20 shots for the same parameters are averaged to obtain more precise values. Energy that is not reflected from the plasma is presumed absorbed, and Fig. 23(a) shows the absorption coefficient, A, the fraction of the power absorbed by the plasma when the rf signal generator is on. Since the errors in the absorption data are small, a polynomial fit is shown, and it is used in determining the temperature. Note also that A is close to unity! Figure 23(a) also shows the noise power received from the plasma, relative to that from the calibrated noise source, ρ. The radiation temperature of the plasma shown in Fig. 23(b) is then determined from the relationship $T_{\mathrm{rad}}=(\rho/A)\,T_{\mathrm{ref}}$. The temperature is 0.5–0.6 eV, and changes only slightly over 400 ms; whereas the plasma density decays by nearly a factor of 10 during this time. The near constancy of the temperature has been observed on most measurements, although the value of the temperature varied between 0.5 and 3.0 eV with different injection conditions. These temperatures are typical of those obtained by other methods.

Because the cylinder radius (2.5 cm) is small compared to the free space wavelength (215 cm) of the radiation, these

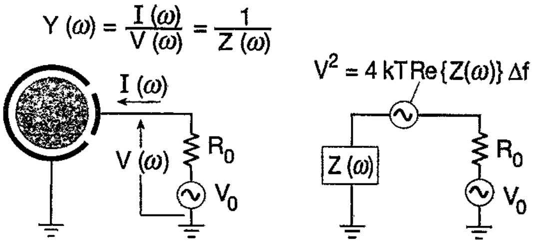

FIG. 24. The model for emission and absorption. Left: electrical schematic of the experiment. Right: equivalent electrical circuit with the plasma replaced by its equivalent noise source and impedance function.

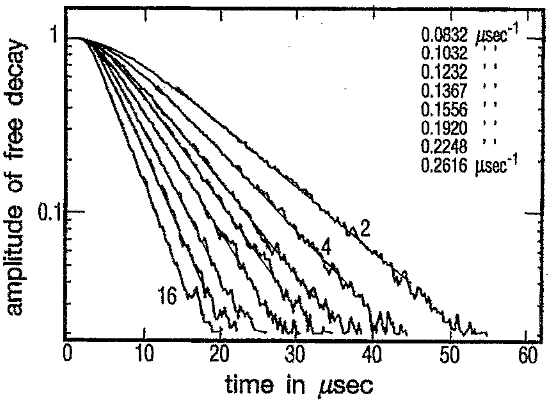

FIG. 26. A semilog plot of the free decay of the $m=1$ mode amplitude versus time when excited by a short resonant burst. Traces are for 2–16 sectors terminated in 50 Ω, indicating that terminating additional sectors *increases* the decay rate.

results can be interpreted in terms of the electric circuit model shown in Fig. 24. If the plasma is at temperature T, the power emitted per unit bandwidth into the load R_0 (50 Ω) is κTA, where κ is Boltzmann's constant and A is the absorption coefficient. The latter is obtained from the equivalent circuit as $A=4R_0R/|R_0+Z(\omega)|^2$, where the impedance function, $Z(\omega)=1/Y(\omega)$, is the inverse of the admittance function and R is the real part of $Z(\omega)$.

One of the surprising results is that the $m=1$ mode absorbs energy at all. The $m=1$ mode is expected, from elementary considerations, to be lossless. Furthermore, as illustrated in Fig. 23(a) the absorption coefficient changes only slightly, while the density decays by nearly an order of magnitude. It is possible to obtain the frequency shift and linewidth versus time of the $m=1$ mode from the Lorentzian fits to the data of Fig. 22. These are shown in Fig. 25. The linewidth is 10–40 kHz, a significant fraction of the frequency shift, 30–180 kHz. Furthermore, the linewidth tracks the density decay. The frequency width of the mode is found from $\Delta\omega=(d\omega_1/dt)\Delta t$, where Δt is the time to sweep through the mode, as determined from Fig. 22, and $d\omega_1/dt$ is the rate of change of the $m=1$ mode frequency. Since the absorption coefficient A is about unity, the plasma is matched to the 50 Ω system, and therefore half the linewidth is due to the external system and the remaining half is *intrinsic* to the plasma.

An independent determination of the linewidth of the $m=1$ cyclotron mode has been made by measuring its decay rate when excited by a short burst at the mode frequency. By adding 50 Ω resistors to various numbers (N) of the octupole sectors, their effect on the damping rate can be found. This is the high-frequency analog of the $m=1$ and $m=2$ low-frequency resistor experiments,[36,42] except that here the external dissipation *increases* the damping, indicating that the mode is a positive energy mode. The result is shown in Fig. 26 and shows clearly that the damping rate increases linearly with N. The minimum value of N is 2, from the source and the receiver, giving a decay time of about 50 μs. To determine the *intrinsic* ($N=0$) damping rate of the mode, the damping rate versus N is plotted and the intercept corresponding to $N=0$ is determined. This result is shown in Fig. 27 for several different densities. The most important conclusions are that the intrinsic damping rate is nonzero, and that, for low densities, the intrinsic damping rate increases with density. The latter is consistent with A, being approximately independent of density.

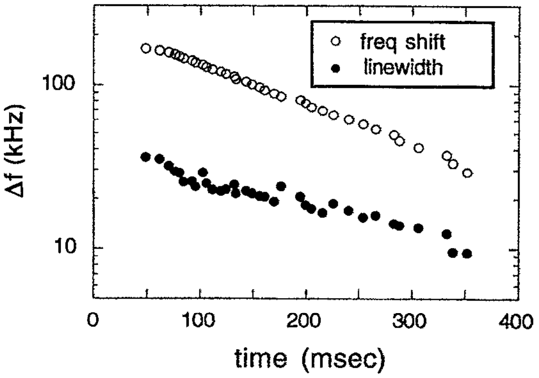

FIG. 25. Experimentally determined frequency downshift and linewidth versus time for the $m=1$ cyclotron mode, as determined from traces similar to those of Fig. 22.

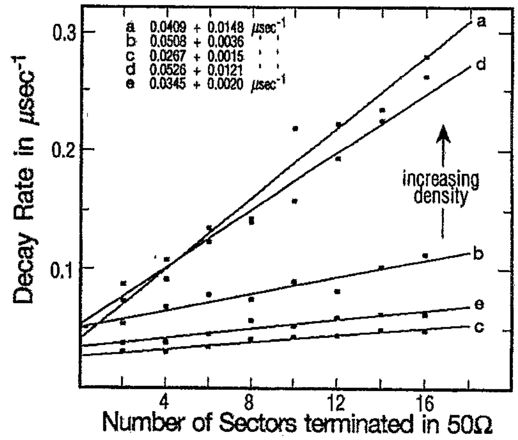

FIG. 27. The measured free decay rate of the $m=1$ mode versus the number of sectors terminated with resistors. The nonzero intercept indicates an *intrinsic* damping of the $m=1$ mode.

VII. DISCUSSION

The experimental results presented above suggest some unresolved issues, which may lead to a still better understanding of the phenomena.

For $m=1$, the cold plasma equations for a non-neutral plasma predict two discrete undamped center of mass modes. The low-frequency mode is observed to be undamped[23] or weakly damped;[52] whereas, the high-frequency mode is strongly damped. This origin of this damping is as yet unexplained.

For $m>1$, the cold plasma equations predict absorption bands (continuum of singular eigenmodes) for *both* the low frequencies, $\omega\sim\omega_0$, and high frequencies, $\omega\sim\omega_c$. However, experimentally, radially trapped Bernstein modes are found in the frequency band in which the high-frequency absorption band is supposed to appear. These require temperature or finite Larmor radius (FLR) effects. However, temperature and FLR effects *appear* to be unimportant for the low-frequency diocotron modes. Why?

For the collisionless damping of low-frequency disturbances in sheared flows, such as those described in Sec. VI, what is the role and importance of viscosity? One normally thinks of viscosity as a dissipative phenomenon, and it was found that external dissipation *reduces* the collisionless damping rate. Does viscosity have the same effect?

Approximate solutions of the Vlasov equation in *sheared* flow, such as those presented by Pearson[53] for neutral cylindrical plasmas and by Prasad *et al.*[54] for a non-neutral slab plasma, are needed for both the high-frequency and low-frequency regimes. In order to carry out such analyses, it is necessary to find slowly evolving self-consistent *sheared* profiles from which to start.

Plasma temperature appears to decay much more slowly than plasma density in pure electron plasmas. This observation needs an explanation. The release of energy through the expansion of the plasma as the density decays probably plays a role in determining the temperature.

ACKNOWLEDGMENTS

I gratefully acknowledge the vital contributions of N. Sateesh Pillai and Michael A. LaPointe to the results described in Secs. IV and VI, respectively. I am also deeply grateful to the late John H. Malmberg and Thomas M. O'Neil for rekindling my interest in this subject and, together with Fred Driscoll, for freely sharing their insights and expertise.

I thank the Office of Naval Research for its support of the research reported here.

[1] L. Brillouin, Phys. Rev. **67**, 260 (1945).
[2] G. G. McFarlane and H. G. Hay, Proc. Phys. Soc. **63**, 409 (1953).
[3] W. W. Rigrod and J. A. Louis, Bell Syst. Technol. J. **33**, 399 (1954).
[4] R. R. Warnecke, P. Guenard, O. Doehler, and B. Epsztein, Proc. Inst. Radio Eng. **43**, 413 (1955).
[5] R. G. E. Hutter, *Beam and Wave Electronics in Microwave Tubes* (Van Nostrand, Princeton, NJ, 1960), see Chaps. 10 and 11.
[6] R. W. Gould, J. Appl. Phys. **28**, 599 (1957); R. W. Gould, Ph.D. thesis, California Institute of Technology, Pasadena, CA, 1956.
[7] H. F. Webster, J. Appl. Phys. **26**, 1386 (1955); R. L. Kyle and H. F. Webster, I.R.E. Trans. Electron. Devices **3**, 172 (1956).
[8] A. J. Theiss, R. A. Mahaffey, and A. W. Trivelpiece, Phys. Rev. Lett. **35**, 1436 (1975).
[9] R. E. Pechacek, C. A. Kapetanakos, and A. W. Trivelpiece, Phys. Rev. Lett. **21**, 1436 (1968); Phys. Fluids **14**, 1555 (1971).
[10] R. H. Levy, Phys. Fluids **8**, 1288 (1965).
[11] R. J. Briggs, J. D. Daugherty, and R. H. Levy, Phys. Fluids **13**, 421 (1970).
[12] R. C. Davidson, *Theory of Nonneutral Plasmas* (Benjamin, Reading, MA, 1974).
[13] R. C. Davidson, *Physics of Nonneutral Plasmas* (Addison–Wesley, Redwood City, CA, 1990).
[14] H. Dehmelt and F. L. Walls, Phys. Rev. Lett. **21**, 127 (1968); H. Dehmelt, Adv. Atom. Molec. Phys. **3**, 53 (1967); G. Graff, Z. Naturforsch. **22**, 1960 (1967); J. Byrne, Proc. R. Soc. London **86**, 801 (1965).
[15] L. S. Brown and G. Gabrielse, Rev. Mod. Phys. **58**, 233 (1986).
[16] R. G. Greaves, M. D. Tinkle, and C. M. Surko, Phys. Plasmas **1**, 1439 (1994).
[17] G. Gabrielse, Sci. Am. **267**, 78 (1992).
[18] J. J. Bollinger, D. J. Wineland, and D. H. E. Dubin, Phys. Plasmas **1**, 1403 (1994).
[19] D. H. E. Dubin, Phys. Rev. Lett. **66**, 2076 (1991).
[20] M. D. Tinkle, R. G. Greaves, C. M. Surko, R. L. Spenser, and G. W. Mason, Phys. Rev. Lett. **72**, 352 (1994).
[21] C. S. Weimer, J. J. Bollinger, F. L. Moore, and D. J. Wineland, Phys. Rev. A **49**, 3842 (1994).
[22] J. H. Malmberg and J. S. deGrassie, Phys. Rev. Lett. **35**, 577 (1975).
[23] J. S. deGrassie and J. H. Malmberg, Phys. Fluids **23**, 63 (1980).
[24] C. F. Driscoll and K. S. Fine, Phys. Fluids B **2**, 1359 (1990).
[25] A. W. Hyatt, C. F. Driscoll, and J. H. Malmberg, Phys. Rev. Lett. **59**, 2975 (1987); also see B. R. Beck, J. Fajans, and J. H. Malmberg, Phys. Rev. Lett. **68**, 317 (1992).
[26] K. S. Fine, C. F. Driscoll, J. H. Malmberg, and T. B. Mitchell, Phys. Rev. Lett. **67**, 588 (1991).
[27] X.-P. Huang and C. F. Driscoll, Phys. Rev. Lett. **72**, 2187 (1994).
[28] *Non-Neutral Plasma Physics*, edited by C. W. Roberson and C. F. Driscoll, AIP Conf. Proc. No. 175 (American Institute of Physics, New York, 1988).
[29] *Non-Neutral Plasma Physics II*, edited by J. Fajans and D. H. E. Dubin, AIP Conf. Proc. No. 331 (American Institute of Physics, Woodbury, 1995).
[30] S. A. Prasad and T. M. O'Neill, Phys. Fluids **27**, 206 (1984).
[31] A. W. Trivelpiece and R. W. Gould, J. Appl. Phys. **30**, 1784 (1959); A. W. Trivelpiece, *Slow-Wave Propagation in Plasma Waveguides* (San Francisco Press, San Francisco, CA, 1967).
[32] R. W. Gould, in Chap. 11 of Ref. 5.
[33] A. J. Peurrung and J. Fajans, Phys. Fluids A **5**, 493 (1993).
[34] C. F. Driscoll, J. H. Malmberg, K. S. Fine, R. A. Smith, X.-P. Huang, and R. W. Gould, in *Plasma Physics and Controlled Nuclear Fusion Research*, Nice, 1988 (International Atomic Energy Agency, Vienna, 1989), Vol. 3, p. 507.
[35] A. Arakawa, J. Comput. Phys. **1**, 119 (1966).
[36] N. Sateesh Pillai and R. W. Gould, Phys. Rev. Lett. **73**, 2849 (1994).
[37] N. G. Van Kampen, Physica **21**, 949 (1955).
[38] K. M. Case, Ann. Phys. **7**, 349 (1959).
[39] L. D. Landau, J. Phys. USSR **10**, 25 (1946).
[40] N. Corngold, Phys. Plasmas **2**, 620 (1995).
[41] D. Bachman and R. W. Gould, Bull. Am. Phys. Soc. **39**, 1738 (1994).
[42] W. D. White, J. H. Malmberg, and C. F. Driscoll, Phys. Rev. Lett. **49**, 1822 (1982).
[43] R. W. Gould, Am. J. Phys. **37**, 585 (1969).
[44] R. W. Gould, T. M. O'Neil, and J. H. Malmberg, Phys. Rev. Lett. **19**, 219 (1967).
[45] R. W. Gould, Phys. Plasmas **2**, 1404 (1995).
[46] R. W. Gould and M. A. LaPointe, Phys. Rev. Lett. **67**, 3685 (1991); Phys. Fluids B **4**, 2038 (1992).
[47] I. B. Bernstein, Phys. Rev. **109**, 10 (1958).
[48] J. V. Parker, J. C. Nickel, and R. W. Gould, Phys. Rev. Lett. **11**, 183 (1963); Phys. Fluids **7**, 1489 (1964).
[49] S. J. Buchsbaum and A. Hasegawa, Phys. Rev. Lett. **12**, 685 (1964); Phys. Rev. **143**, 303 (1966).
[50] R. L. Stenzel and R. W. Gould, Phys. Rev. Sci. Inst. **40**, 1461 (1969).
[51] D. J. Wineland and H. G. Dehmelt, J. Appl. Phys. **46**, 919 (1975).
[52] B. Cluggish and C. F. Driscoll, Bull. Am. Phys. Sci. **38**, 1736 (1994); B. Cluggish and C. F. Driscoll, "Transport and damping from rotational pumping in magnetized electron plasmas," to appear in Phys. Rev. Lett.
[53] G. A. Pearson, Phys. Fluids **9**, 2454, 2464 (1966).
[54] S. A. Prasad, G. J. Morales, and B. D. Fried, Phys. Fluids **30**, 3093 (1987).